Development of the flight model of a tilt-body MAV

L. R. Lustosa, F. Defay, and J. M. Moschetta *
ISAE - Institut Supérieur de l'Aéronautique et de l'Espace, University of Toulouse

ABSTRACT

This article presents the results of a wind tunnel campaign for a tilt-body UAV, the MAVion. The objective of this campaign is to develop a simplified flight model for use in control systems design and implementation. In order to achieve precise flight control during transition, stationary and cruise modes, the aerodynamic coefficients are identified for a wide flight envelope of angle of attack and sideslip. Additionally, the equilibrium transition is studied and the results validate the MAVion design. Moreover, an analysis of performance on aerodynamics due to addition of winglets in this platform is carried out.

1 INTRODUCTION

The use of Micro Air Vehicles (MAVs) for recognition missions in complex urban environments require the design of new MAV configurations capable of both horizontal and vertical flights. A typical mission scenario would consist of flying to a remote location, loiter and collect sensor data for an extended period of time, then hover to identify targets and possibly enter buildings, land, take off, without human assistance.

Typical fixed wing MAV configurations are appropriate to complete outdoor surveillance missions because they can cope with adverse windy conditions and provide a fairly good range as opposed to VTOL configurations. However, they are often limited in their practical application due to their intrinsic difficulty to sustain low-speed or hover flight. On the other hand, conventional VTOL MAV configurations such as multirotor platforms offer the capability to persistently survey an area by hovering or by achieving a perch-and-stare approach. However, VTOL configurations usually suffer from limited endurance and fail to efficiently sustain high speed flight. Therefore, it is of interest to combine the fixed and rotary wing capabilities into a single convertible-rotor aircraft.

In order to achieve either translation flight or vertical flight, different options are available. One is to directly tilt the rotors or the wing located in the rotor slipstream such as in the V-22 "Osprey" configuration. In the field of MAVs, the AVIGLE developed at Aachen University is an example of such a concept which requires an additional rotor above the horizontal tail in order to control the pitching moment [1]. Furthermore, it requires a tilting mechanism in the airframe which leads to a significant weight penalty. Another approach consists of designing a fixed-wing configuration which can be tilted when needed so as to perform hover flight in a "prop hanging" mode. Such a tilt-body concept has been around for over half a century with the famous Convair XFY-1 "Pogo" developed and flight tested in the 1950s. Such a tail-sitter mini-UAV called "Vertigo" was developed and flown in 2006 at ISAE and further miniaturized in collaboration with the University of Arizona to provide the "Mini-Vertigo", a 30-cm span coaxial-rotor MAV capable of transition flight [2]. However, the coaxial rotor driving mechanism represents an additional weight and a technological limitation to design smaller versions. Furthermore, because of its limited aspect ratio, the Mini-Vertigo generates a fairly high induced drag in cruise conditions. In view of improving the aerodynamic performance in horizontal flight and simplifying the rotor mechanism, a new tilt-body configuration based on the bimotor flying wing has been designed. The MAVion has been initially designed to be a reasonably good airplane, capable of flying outdoors and easy to replicate as opposed to more complicated tail-sitters [3]. The main design guidelines were simplicity and transition flight capacity. The use of tandem rotors in tractor configuration allows for an additional degree of freedom which provides control in yaw and proved to ensure both hover and horizontal flight without resorting to complex tilting mechanisms [4]. The aerodynamic efficiency of the MAVion elevons is guaranteed over the whole transition flight range since in hover, when the freestream flow is drastically decreased, the propeller slipstream maintains the elevator aerodynamic efficiency. Previous studies have investigated the problem of a propeller at very high angle of attack [5] and the propeller-wing interaction [6, 7] while few studies have been conducted to actually provide a full model of the aircraft in transition flight. It is the purpose of the present paper to describe the development of a full aircraft model based on a new wind tunnel campaign in which a broad range of angles of attack and slip angles have been tested.

2 TILT-BODY MAV DYNAMICS MODELING

2.1 Aerodynamic forces and moments

Aerodynamic forces and moments are described in this work in 2 different orthogonal coordinate systems, namely, body-fixed (Figure 1) and wind systems. An inviscid incompressible flow is assumed and, consequently, the aerodynamic coefficients for the MAVion $C_{\square}(\alpha, \beta, \delta_1, \delta_2)$ are dependent on angle of attack α, sideslip β and elevons deflection δ_i, and

*Email address(es): (leandro-ribeiro.lustosa, francois.defay, jean-marc.moschetta)@isae.fr

are related to aerodynamic forces and moments by

$$\begin{array}{ll} F_x = C_x q_\infty S & M_x = C_{mx} q_\infty S b \\ F_y = C_y q_\infty S & M_y = C_{my} q_\infty S \bar{c} \\ F_z = C_z q_\infty S & M_z = C_{mz} q_\infty S b \end{array} \quad (1)$$

and

$$\begin{array}{ll} F_D = C_D q_\infty S & M_d = C_d q_\infty S b \\ F_Y = C_Y q_\infty S & M_y = C_y q_\infty S \bar{c} \\ F_L = C_L q_\infty S & M_l = C_l q_\infty S b \end{array} \quad (2)$$

where

$$q_\infty = \frac{1}{2}\rho_\infty V_\infty^2 \quad (3)$$

and q_∞, ρ_∞ and V_∞ denote, respectively, free-stream dynamic pressure, density and velocity, whereas S denotes MAVion reference area defined by the product of its mean aerodynamic chord $\bar{c}$ and its wing-span s. Moments in both coordinate systems are taken with respect to the center of mass.

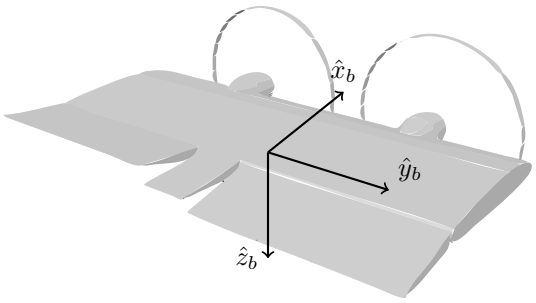

Figure 1: Perspective view and body-axis definition.

In the present work, the $C_x, C_y, C_z, C_{mx}, C_{my}, C_{mz}$ aerodynamic coefficients are identified by means of a wide-envelope wind tunnel campaign in α and β and can be related to wind-fixed coordinates by a rotation transformation, namely

$$D_w^b = \begin{bmatrix} -cos(\beta)cos(\alpha) & -sin(\beta) & -cos(\beta)sin(\alpha) \\ -sin(\beta)cos(\alpha) & cos(\beta) & -sin(\beta)sin(\alpha) \\ -sin(\alpha) & 0 & -cos(\alpha) \end{bmatrix} \quad (4)$$

so that

$$\mathbf{C}_w \triangleq \begin{pmatrix} C_D \\ C_Y \\ C_L \end{pmatrix} = D_w^b \begin{pmatrix} C_x \\ C_y \\ C_z \end{pmatrix} \triangleq D_w^b \mathbf{C}_b \quad (5)$$

and

$$\mathbf{C}_{m,w} \triangleq \begin{pmatrix} C_d \\ C_y \\ C_l \end{pmatrix} = D_w^b \begin{pmatrix} C_{mx} \\ C_{my} \\ C_{mz} \end{pmatrix} \triangleq D_w^b \mathbf{C}_{m,b} \quad (6)$$

2.2 *Propulsion forces and moments*

Similarly to the aerodynamic model development, a dimensional analysis is performed assuming little influence of viscous effects and Froude number and it leads to MAVion forces T_i and moments Q_i applied at the propeller i given by

$$T_i = \rho n_1^2 D^4 C_T(J_i) \quad (7)$$

and

$$Q_i = \rho n_1^2 D^5 C_Q(J_i) \quad (8)$$

where

$$J_i = \frac{V_{\infty,N}}{n_i D} \quad (9)$$

and n_i, D, C_T, J_i denote motor speed in revolutions per second, propeller disk diameter, coefficients of thrust and moment, and advance coefficient. C_T and C_Q are modelled as a linear relation in J_i as previously studied in [8].

2.3 *Propeller downwash effects*

In horizontal flight, the propeller system pushes air downstream in order to balance small drag forces and creates a downwash slipstream towards the aerodynamic surfaces which can usually be disregarded due to its small strength and influence on the overall forces system. However, in transition mode or vertical flight, a more influent downwash slipstream is created to overcome the weight of the aircraft. This slipstream interacts with the aerodynamic surfaces and creates induced forces and moments.

The fundamental idea applied in this work is to divide the aerodynamic surfaces in two parts, namely, wet and dry parts (see Figure 2). The dry part has an area S_{dry} whereas the wet part area S_{wet} is such that, by the disk actuator theory,

$$S_{wet} = \frac{1}{2}S \quad (10)$$

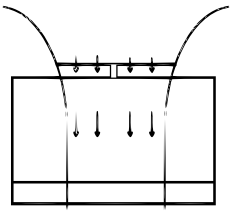

Figure 2: Propeller wake illustration.

Independence between areas S_{dry} and S_{wet} is assumed such that the dry area is unaffected by the propulsion system and its empirically modeled in the light of the blade element theory as

$$\mathbf{F}_b = q_\infty S_{dry} \mathbf{C}_b(\alpha, \beta, \delta_1, \delta_2) \quad (11)$$

and

$$\mathbf{M}_b = q_\infty S_{dry} \begin{bmatrix} b & 0 & 0 \\ 0 & \bar{c} & 0 \\ 0 & 0 & b \end{bmatrix} \mathbf{C}_{m,b}(\alpha, \beta, \delta_1, \delta_2) \quad (12)$$

whereas the wet part is computed as

$$\mathbf{F}_b = q_{\infty,ind} S_{dry} \mathbf{C}_b(\alpha_{ind}, \beta, \delta_1, \delta_2) \quad (13)$$

and

$$\mathbf{M}_b = q_{\infty,ind} S_{dry} \begin{bmatrix} b & 0 & 0 \\ 0 & \bar{c} & 0 \\ 0 & 0 & b \end{bmatrix} \mathbf{C}_{m,b}(\alpha_{ind}, \beta, \delta_1, \delta_2) \quad (14)$$

where α_{ind} and $q_{\infty,ind}$ capture the influence of the wake flow on the aerodynamic surfaces and are modelled as [2]

$$\alpha_{ind} = \alpha - sin^{-1}\Big(\frac{wcos\beta sin\alpha}{V_{\infty,ind}}\Big) \quad (15)$$

and

$$q_{\infty,ind} = \frac{1}{2}\rho V_{\infty,ind}^2 \quad (16)$$

where $V_{\infty,ind}$ is given by

$$V_{\infty,ind}^2 = (w + V_\infty cos\beta cos\alpha)^2 + (V_\infty sin\beta)^2 + \\ + (V_\infty cos\beta sin\alpha)^2 \quad (17)$$

and w is the solution of the following quartic

$$w^4 + 2V_\infty cos\alpha cos\beta w^3 + V_\infty^2 w^2 = \Big(\frac{2T_i}{\pi\rho D^2}\Big)^2 \quad (18)$$

3 Wind Tunnel Campaign

Due to the convertible nature of the vehicle, a 6-component (3-dimensional forces and moments) wide angle of attack and sideslip envelope wind tunnel campaign took place to validate the 6 degree-of-freedom theoretical model.

3.1 SabRe Wind Tunnel and Balance

The experiments were ran at the SabRe closed-loop wind tunnel (Figure 3) located at ISAE and capable of delivering low Reynolds stable and uniform flow at a wind velocity range of 2 to 25 m/s, thus ideal for experimenting full-span micro air vehicles.

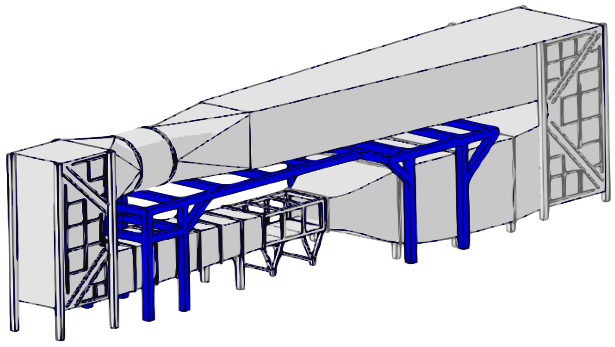

Figure 3: SabRe Wind Tunnel.

Forces and moments were measured by means of a 5-component internal balance (2-dimensional forces and 3-dimensional moments measured in the balance body coordinate system). Therefore, the desire of a full 6-component study calls for 2 different internal balance configurations (see Figure 4) for every set of experimented $\{\alpha, \beta, V_\infty, \omega_1, \omega_2, \delta_1, \delta_2\}$. Therefore a duplicity of values for $\{F_{bx}, M_{bx}, M_{by}, M_{bz}\}$ arrives and it is used for evaluating repeatability and detecting procedural errors.

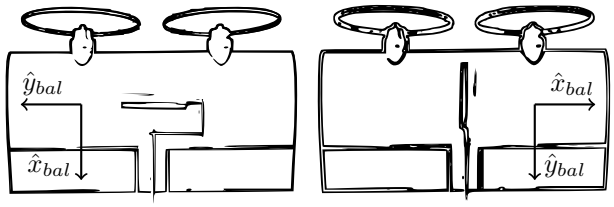

Figure 4: Two internal balance configurations.

Comparing the MAVion and balance coordinates systems (Figures 1 and 4) in both configurations, and assuming MAVion and balance perfect alignment, it can be readily seen that

$$\begin{pmatrix} F_{bx} \\ F_{by} \\ F_{bz} \end{pmatrix} = \begin{bmatrix} -1 & 0 & 0 \\ 0 & -1 & 0 \\ 0 & 0 & -1 \end{bmatrix} \begin{pmatrix} X \\ Y \\ Z \end{pmatrix} \quad (19)$$

and

$$\begin{pmatrix} M_{bx} \\ M_{by} \\ M_{bz} \end{pmatrix} = \begin{bmatrix} 1 & 0 & 0 \\ 0 & 1 & 0 \\ 0 & 0 & 1 \end{bmatrix} \begin{pmatrix} L \\ M \\ N \end{pmatrix} \quad (20)$$

for balace configuration 1, whereas

$$\begin{pmatrix} F_{bx} \\ F_{by} \\ F_{bz} \end{pmatrix} = \begin{bmatrix} 0 & -1 & 0 \\ 1 & 0 & 0 \\ 0 & 0 & -1 \end{bmatrix} \begin{pmatrix} X \\ Y \\ Z \end{pmatrix} \quad (21)$$

and

$$\begin{pmatrix} M_{bx} \\ M_{by} \\ M_{bz} \end{pmatrix} = \begin{bmatrix} 0 & 1 & 0 \\ -1 & 0 & 0 \\ 0 & 0 & 1 \end{bmatrix} \begin{pmatrix} L \\ M \\ N \end{pmatrix} \quad (22)$$

for balance configuration 2. The opposite signs in force and moment matrix transformation are due to balance manufacturer left-hand moment convention notwithstanding MAVion right-handed coordinate system.

The MAVion model is rigidly mounted on a movable platform with 2 degrees-of-freedom with respect to the wind, namely, yaw θ_1 and pitch θ_2 such that

$$\begin{cases} \frac{-\pi}{2} < \theta_1 < \frac{\pi}{2} \\ \frac{-\pi}{6} < \theta_2 < \frac{\pi}{6} \end{cases} \quad (23)$$

due to mechanical restrictions. Since the flight envelope includes horizontal flight (θ_2 near 0) and vertical flight (θ_2 near

$\pi/2$), an additional wind tunnel set-up difficulty arises due to limitations in the total excursion of θ_2. Such shortcoming calls for additional testing configurations illustrated by Figure 5. In configuration M, large angles of sideslip are achievable and the following direct relations between wind and platform angles can be written

$$\alpha = \theta_2 \tag{24}$$

and

$$\beta = \theta_1 \tag{25}$$

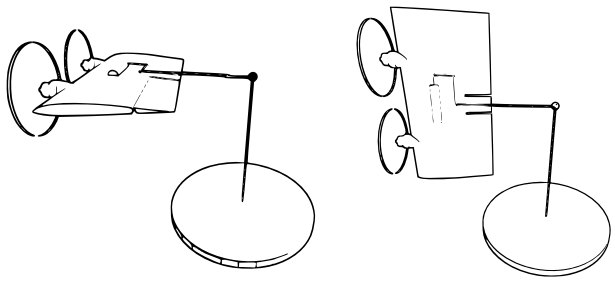

Figure 5: Wind tunnel configurations. On the left, configuration M. On the right, configuration M'.

Complementary, configuration M' delivers high angles of attack, but the relation between wind and platform angles is not obvious anymore, and a series of equivalent transform rotations will deliver

$$\alpha = -tan^{-1}(tan\theta_1 sec\theta_2) \tag{26}$$

$$\beta = sin^{-1}(cos\theta_1 sin\theta_2) \tag{27}$$

Finally, several configurations in this study suffer from potential ground and blockage effects due to high angles of attack. Previous work demonstrated that ground effects are negligible, and as so, they will be disregarded herein. However, future theoretical and computational studies are planned to account for forces and moments errors due to blockage in this campaign.

3.2 Wind Tunnel Model and Acquisition System

An adapted MAVion was manufactured for wind tunnel campaign purposes (Figure 12). Its main objectives were to enable rigid installment of the internal balance in both configurations and to provide a non-deformable airfoil section to aerodynamic identification. Figure 6 illustrates the electronics counterpart.

Two servo-motors are responsible for elevons deflection. Two potentiometers are installed in both elevons as to accurately measure elevon deflections δ_i. Notice that the potentiometer inside the servo dedicated to move the elevon could perform similar task, but it is more inaccurate due to rod deformations and servo-control errors.

The propulsion system, namely, two brushless CC motors equipped with speed controllers, which communicate by I2C

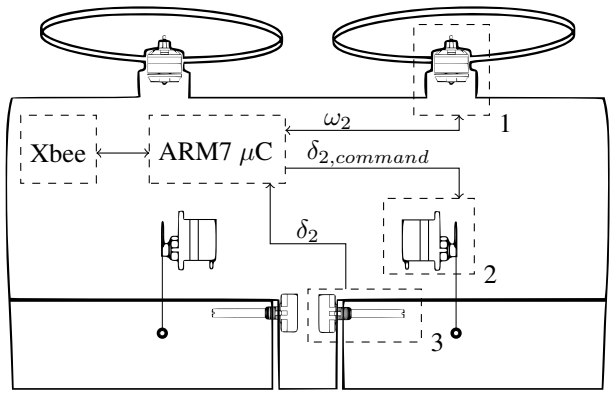

Figure 6: MAVion wind tunnel model instrumentation.

with MAVion onboard computer, controls and measures the rotation speed ω_i of each helix.

The wind tunnel ground station (Figure 7) communicates with MAVion onboard computer by means of a wireless XBee connection in order to minimize cables and their induced forces and torques on the system due to their intrinsic stiffness. The wind tunnel ground station is then responsible for commanding motor speeds and elevons deflections in an open-loop configuration, receiving telemetry data from MAVion (ω_i and δ_i, which may be different from commanded values due to the open-loop control nature), receiving data from balance and registering all measured values.

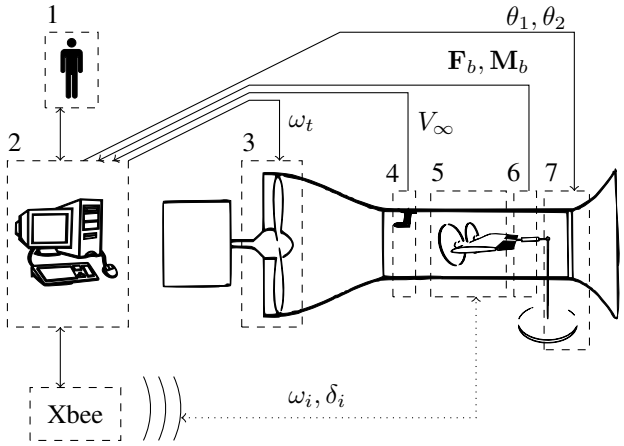

Figure 7: Wind tunnel acquisition system set-up.

Two distinct methodologies were used to collect wind tunnel data, namely, equilibrium transition study and exploration study. In both, the wind tunnel operator set the operating conditions of tunnel and MAVion, collected sensors measurements and registered them all in a line of a table corresponding to an experimental trial. The operating conditions included wind velocity V_∞, angle of attack α and sideslip β, elevons deflection δ_i, propulsion motors speed ω_i. The sen-

sors measurements included flow temperature and pressure, precise flow speed, elevons potentiometers readings, propulsion motors controllers rotational speed, and 5-component balance forces and moments.

3.3 Equilibrium Transition Study

Equilibrium points, i.e. flight condition points $(\alpha, \beta, V_\infty, \delta_1, \delta_2, \omega_1, \omega_2)$ in which the sum of gravitational, aerodynamic and propulsion forces and moments are null, are particularly interesting for analyzing flight envelope and steady flight conditions. By means of the wind tunnel campaign, it will be experimentally shown that exists a n-tuple $(V_\infty, \delta_1, \delta_2, \omega_1, \omega_2)$ such that longitudinal equilibrium is achieved for each α throughout the entire $[0^o, 90^o]$ angle of attack envelope and thus the MAV design allows for a quasi-static[1] equilibrium transition between horizontal and vertical mode. Therefore, when there's no wind, transitioning between horizontal and vertical modes can be achieved by climbing over the target until the relative ground speed reaches zero (Fig. 8). However, when there is some wind, hovering with respect to a target on the ground requires an equilibrium flight with non-zero vehicle velocity with respect to the wind (Fig. 8) and the ability to hover in windy conditions is limited by the vehicle maximum velocity with respect to the wind.

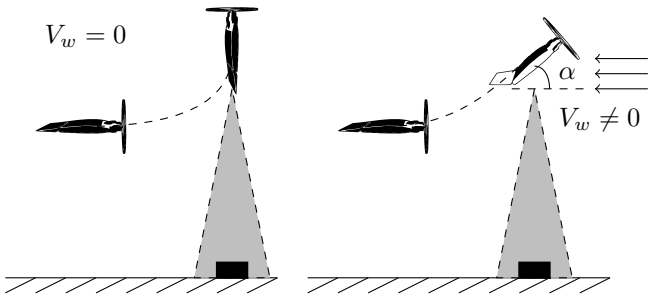

Figure 8: Quasi-static equilibrium transition maneuvers and hovering over ground target under non-windy (left) and windy (right) conditions.

Equilibrium points were studied in this campaign by following the general guidelines stated by [4] for longitudinal flight, i.e., $\beta = 0$. The fundamental idea is to, for each sampled α, search for values of $V_\infty, \delta_i, \omega_i$ that will deliver aerodynamic/propulsion forces and moments (notice gravitational suppression) that will cancel gravitational forces and moments on the *flying* model, which has a different mass distribution than the wind tunnel model that is not meant to fly. The desired flying model mass distribution is such that the center of mass is longitudinally located at a position $0.15c$ away from the leading edge and is motivated by a 10% stability margin controls requirement.

At each α, flow velocity was modified until lift was balanced by weight. Next, the propulsion motors velocity was set such that drag was equal to thrust. Then, the elevons were deflected in such a way to eliminate pitching moment. However, modifying one variable unbalances the other equilibria and an iterated scheme is proposed for reaching longitudinal equilibrium. Once it is found, all wind tunnel data is recorded as a new point in the equilibrium transition experimental table. Current and voltage measurements also took place to study power requirements. The results can be seen in Figure 9.

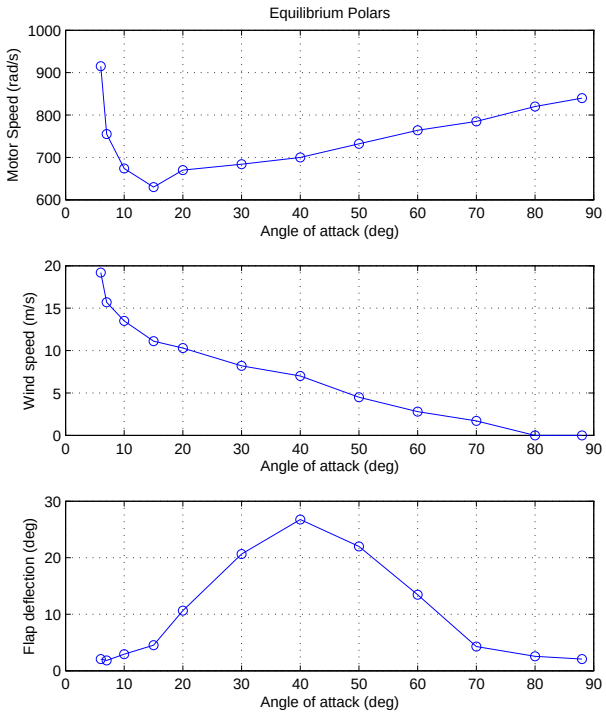

Figure 9: Equilibrium transition study.

The results show that the vehicle is actually capable of sustaining equilibrium flight during the whole transition phase between 0 and 20 m/s, which means that it is capable of hovering with respect to the ground for lateral wind speeds ranging from 0 to 20 m/s (Figure 9B). Figure 9A indicates that the motor regime is limited by two extreme cases: hover at 90^o angle of attack and fast cruise speed at 5^o angle of attack. Finally, the elevator deflection angle is plotted as a function of the angle of attack, showing a maximum deflection value of 27^o at 40^o angle of attack, within the range of the elevator aerodynamic efficiency. This confirms that because the elevons are placed within the propeller slipstream,

[1] Quasi-static equilibrium transition additionally allows us to disregard aerodynamic derivatives effects in the MAVion dynamic model. However, if a faster transition is required, the aerodynamic derivatives effects can no longer be neglected and should be included in the differential equations that model the system. They also should be identified by theory, experimental flights or a different type of wind tunnel campaign.

control in pitch is maintained throughout the entire transition flight phase.

3.4 Exploration Study

Data were also taken by independently setting the angle of attack, sideslip, motor speed and flap deflection to the values illustrated by tables 1 and 2. All combinations were exhaustively tried and the associated forces and moments registered.

θ_2	$-10, 0, 10, 20, 30$	deg
θ_1	$0, 30, 60, 90$	deg
ω_i	$0, 400, 800$	rad/s
(δ_1, δ_2)	$(-30, \pm 30), (-15, \pm 15), (0, 0),$ $(15, \pm 15), (30, \pm 30)$	$deg \times deg$

Table 1: Flight variables tested in configuration M.

θ_2	$0, 30$	deg
θ_1	$0, 30, 40, 50, 60, 70, 80, 90$	deg
ω_i	$0, 400, 800$	rad/s
(δ_1, δ_2)	$(-30, \pm 30), (-15, \pm 15), (0, 0),$ $(15, \pm 15), (30, \pm 30)$	$deg \times deg$

Table 2: Flight variables tested in configuration M'.

3.5 Model parameters identification and validation

The strategy for model identification is based on aerodynamic coefficients $\mathbf{C}_b(\alpha,\beta,\delta_i)$ and $\mathbf{C}_{m,b}(\alpha,\beta,\delta_i)$ 4^{th} order polynomial curve fitting of the data collected in all experimental trials with no propulsion. Afterwards, in order to validate the model, the resulting aerodynamic interpolated data is used alongside the propulsion model described in section 2.2 to predict forces and moments measured in powered model tests. Theoretical and experimental results are compared in Figure 10.

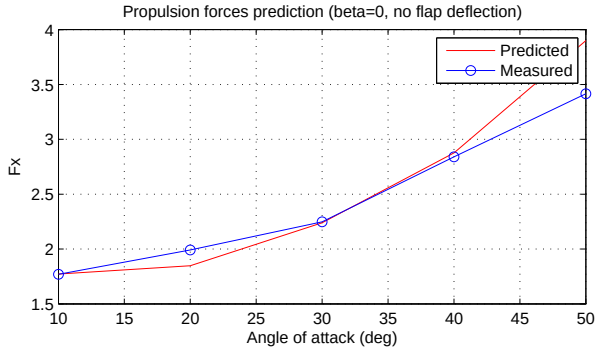

Figure 10: Axial force validation.

The results show accordance between model and measurements for small angles of attack. However, it fails to predict propulsion components at very high angles of attack. Nevertheless, future work will check whether propulsion model parameters can be adapted to better fit the measurements.

3.6 Winglets study

An outdoor version of the MAVion has been equipped with winglets which act as vertical tails and provide positive stiffness in roll (Figure 12). The triangular shape of the winglets has been designed in order to keep the elevon tips in contact with the winglets even when fully tilted. By doing so, the elevon tips always remain limited by the winglets, which eventually reduces tip losses. As illustrated by Figure 11A which shows the pitching moment gradient with respect to the elevator deflection angle for varying values of the angle of attack, the elevator efficiency is increased when winglets are added. Interestingly, winglets significantly enhance the elevon efficiency particularly in the middle of transition (around 40^o angle of attack) when the elevons are tilted at their maximum value (see Fig. 9C). Also, it is noticed that the additional skin friction drag due to the additional winglets wetted area is not visible on the aerodynamic polar (Figure 11B) while the induced drag is significantly decreased at high lift forces. On a practical viewpoint, adding winglets may be useful to protect the elevons and to provide a natural landing device.

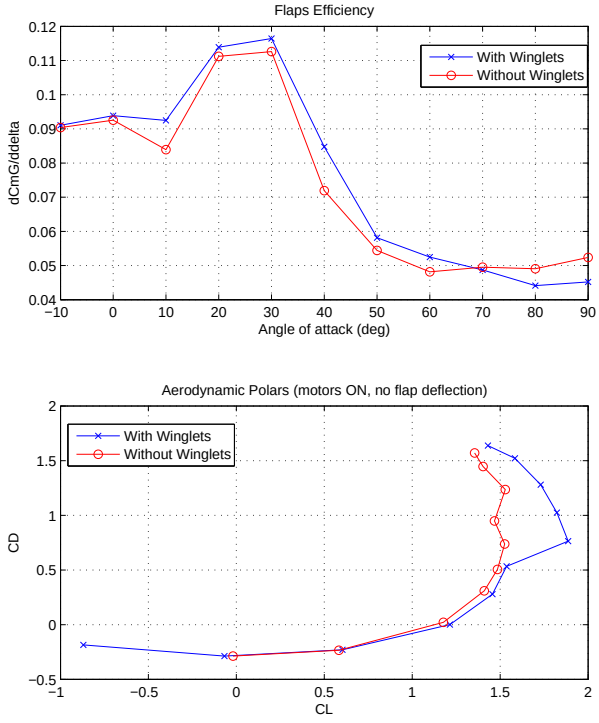

Figure 11: Winglets study.

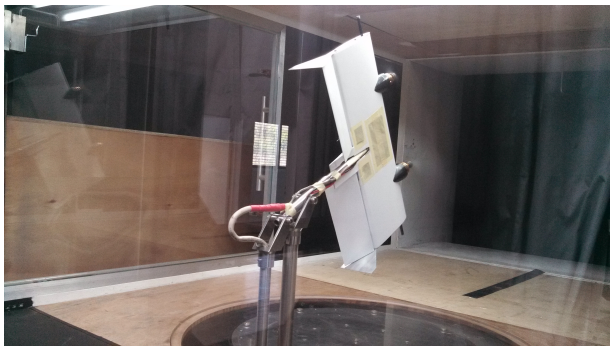

Figure 12: MAVion with winglets version in SabRe.

4 Conclusion

In this paper a flight dynamics model for a tilt-body MAV was described. After an overview of the aerodynamics principles that govern the proposed model, a complete wind tunnel campaign is presented. The materials and the set-up procedure for the campaign were described for the MAVion. The equilibrium transition was performed and studied, and validated the MAV design. Additionally, an analysis on the effect of winglets over the overall aerodynamics performance of MAVion is carried out. Finally, the identified model will be used as basis for the flight control systems design of a flying MAVion platform that is currently being manufactured at ISAE.

Acknowledgements

The authors gratefully acknowledge the Conselho Nacional de Desenvolvimento Científico e Tecnológico, CNPq, (Brazilian National Science Foundation), for partial financial support for this work through the "Ciência sem Fronteiras" program.

References

[1] J. Holsten, T. Ostermann, and D. Moormann. Design and wind tunnel tests of a tiltwing uav. *CEAS Aeronautical Journal*, 2(1-4):69–79, 2011.

[2] S. Shkarayev, B. Bataille, and J.M. Moschetta. Aerodynamic design of micro air vehicles for vertical flight. *Journal of Aircraft*, 45(5):1715–1724, 2008.

[3] R.H. Stone. Aerodynamic modeling of the wingpropeller interaction for a tail-sitter unmanned air vehicle. *Journal of Aircraft*, 45(1):198–210, 2008.

[4] M. Itasse, J.M. Moschetta, Y. Ameho, and R. Carr. Equilibrium transition study for a hybrid mav. *International Journal of Micro Air Vehicles*, 3(4):229–245, 2011.

[5] C. Stahlhut and J. Leishman. Aerodynamic design optimization of proprotors for convertible rotor concepts. *Proceedings of the 68th American Helicopter Society International Annual Forum*, pages 592–616, 2012.

[6] D. Hunsaker and D. Snyder. A lifting-line approach to estimating propeller/wing interactions. *AIAA paper 2006-3466, 24th Applied Aerodynamics Conference, 5 - 8 June 2006, San Francisco, California*, 2006.

[7] B.J. Gamble and M.F. Reeder. Experimental analysis of propellerwing interactions for a micro air vehicle. *Journal of Aircraft*, 46(1):65–73, 2009.

[8] M. P. M. a. L. S. Miller. Propeller performance measurement for low reynolds. *Wichita State University, Wichita, Kansas*, 2006.